The Astrophysical Journal, 770:61 (12pp), 2013 June 10 doi:10.1088/0004-637X/770/1/61

THE IMACS CLUSTER BUILDING SURVEY. I. DESCRIPTION OF THE SURVEY AND ANALYSIS METHODS*

Augustus Oemler, Jr.[1], Alan Dressler[1], Michael G. Gladders[2], Jane R. Rigby[3], Lei Bai[4], Daniel Kelson[1], Edward Villanueva[1], Jacopo Fritz[5], George Rieke[6], Bianca M. Poggianti[7], and Benedetta Vulcani[7,8]
[1] The Observatories of the Carnegie Institution for Science, 813 Santa Barbara St., Pasadena, CA 91101-1292, USA; oemler@obs.carnegiescience.edu
[2] Department of Astronomy and Astrophysics, University of Chicago, Chicago, IL 60637, USA
[3] Observational Cosmology Lab, NASA Goddard Space Flight Center, Greenbelt, MD 20771, USA
[4] Department of Astronomy and Astrophysics, University of Toronto, 50 St. George Street, Toronto, ON M5S 3H4, Canada
[5] Sterrenkundig Observatorium, Universiteit Gent, Krijgslaan 281 S9, B-9000 Gent, Belgium
[6] Steward Observatory, University of Arizona, Tucson, AZ 8572, USA
[7] INAF-Osservatorio Astronomico di Padova, Vicolo dell'Osservatorio 5, I-35122 Padova, Italy
[8] Department of Astronomy, Padova University, Vicolo Osservatorio 3, I-35122 Padova, Italy
Received 2012 August 10; accepted 2013 January 28; published 2013 May 24

ABSTRACT

The IMACS Cluster Building Survey uses the wide field spectroscopic capabilities of the IMACS spectrograph on the 6.5 m Baade Telescope to survey the large-scale environment surrounding rich intermediate-redshift clusters of galaxies. The goal is to understand the processes which may be transforming star-forming field galaxies into quiescent cluster members as groups and individual galaxies fall into the cluster from the surrounding supercluster. This first paper describes the survey: the data taking and reduction methods. We provide new calibrations of star formation rates (SFRs) derived from optical and infrared spectroscopy and photometry. We demonstrate that there is a tight relation between the observed SFR per unit B luminosity, and the ratio of the extinctions of the stellar continuum and the optical emission lines. With this, we can obtain accurate extinction-corrected colors of galaxies. Using these colors as well as other spectral measures, we determine new criteria for the existence of ongoing and recent starbursts in galaxies.

Key words: galaxies: clusters: general – galaxies: evolution – galaxies: photometry – galaxies: star formation

Online-only material: color figures

1. INTRODUCTION

That the properties of galaxies differ with environment has been recognized at least since Hubble (1936). That much of the difference between clusters and the field is of recent origin has been known since Butcher & Oemler (1978). However, the mechanisms that have produced these population differences are still in dispute. Many processes have been suggested which are capable of transforming field-like populations into the predominantly early Hubble types seen in clusters today. These include gas stripping by galaxy–galaxy collisions (Spitzer & Baade 1951), gas stripping by ram pressure from the intracluster medium (Gunn & Gott 1972), a shutoff in gas replenishment (Larson et al. 1980), tidal shocks due to either the cluster core (Byrd & Valtonen 1990; Henriksen & Byrd 1996), unvirialized subclusters (Gneiden 2003), or other galaxies (Richstone & Malmuth 1983; Icke 1985; Moore et al. 1996), and galaxy–galaxy mergers (Dressler et al. 1999; van Dokkum et al. 1999). Since all these processes produce, by design, the same outcome, and have, again by design, a qualitatively similar dependence on environment, distinguishing between them is challenging at best. Given that most extant observations consist of snapshots at one epoch of the cores of individual clusters, it is hardly surprising that the responsible process(es) have still not been unambiguously identified.

The IMACS Cluster Building Survey is an attempt to resolve this problem by following the evolution of galaxies as they move from the supercluster environment, through the infall stage, and end finally with incorporation into the virialized central cluster. It takes advantage of the very wide field and high multiplexing of the IMACS spectrograph on the Baade Telescope (Dressler et al. 2011), which allow one to observe, in one exposure, hundreds of galaxies over a 30′ field, equivalent to a circle with radius of about 5 Mpc surrounding a cluster at redshift 0.4. The goal is to identify the changes that occur in galaxies as they move from field-like environments into increasingly dense and massive assemblies. The much longer baselines of time and environment which these data provide should help distinguish between the various candidate processes for transforming galaxies.

In this paper we describe the design and execution of the survey, up through the production of redshifts, luminosities, colors, masses, and star formation rates (SFRs) of galaxies. We describe new calibrations of SFRs based on optical and infrared photometry and spectroscopy and we discuss several methods for detecting starbursts using the available data. The immediately following papers (Dressler et al. 2013, Paper II; Oemler et al. 2013, Paper III; Gladders et al. 2013, Paper IV) discuss certain aspects of the behavior of galaxies in the cluster and supercluster environment, and the evolution of the field galaxy population. Two papers using ICBS data to analyze environmental variations in the mass function of galaxies have already been completed (Vulcani et al. 2012, 2013). Future papers will address other aspects of both the field and cluster populations. Throughout this and following papers we shall assume cosmological parameters of $H_0 = 71$, $\Omega_{\rm matter} = 0.27$, $\Omega_{\rm tot} = 1.0$.

2. OBSERVATIONS

We wish to map a group of rich intermediate redshift clusters including still-forming objects unlikely to be discovered by

* This paper includes data gathered with the 6.5 m Magellan Telescopes located at Las Campanas Observatory, Chile.

Table 1
Intermediate Redshift Cluster Fields

Cluster	α	δ
RCS0221	$2^h21^m48^s$	$-03°46'$
RCS1102	$11^h02^m36^s$	$-04°40'$
SDSS0845	$8^h45^m30^s$	$+03°27'$
SDSS1500	$15^h00^m30^s$	$+01°53'$

X-ray searches. To do this we use the cluster red-sequence detection method (Gladders & Yee 2000), applied to data from the Red-Sequence Cluster Survey (RCS; Gladders & Yee 2005) and the Sloan Digital Sky Survey (SDSS; York et al. 2000) Data Release 2 (DR2). The RCS data are R_c and z' imaging to a depth sufficient to detect clusters to $z \sim 1.4$, more than sufficient to find clusters at the redshift considered here. The SDSS data are much shallower, but sufficient to find rich/massive clusters at the redshift of interest.

Approximately 50 deg^2 of the RCS imaging are readily visible from the Las Campanas Observatory and we initially searched this area for candidate rich clusters in the desired $0.3 < z < 0.5$ redshift range. Clusters were detected as over-densities on the sky and in color and magnitude space. The richest systems were considered as candidates for the ICBS program. The lack of sufficient RCS imaging area visible from the Southern Hemisphere at 6^h to 9^h and 14^h to 20^h forced us to use the SDSS DR2 data as a secondary source for rich cluster candidates. In order to ensure a reasonable match in mass between the two cluster sub-samples, we restricted our attention in the SDSS to areas of low-extinction sky comparable in size to the RCS search area, at two right ascensions (RAs) selected to facilitate the extensive ICBS data collection. The total comoving volume covered by this search is equal to that in the two Galactic caps out to a redshift $z \sim 0.055$, and should, therefore, include a number of rich clusters comparable to those found in local surveys.

We identified five fields which, from the RCS or from our analysis of the SDSS data, appeared to contain very rich clusters at redshifts between 0.3 and 0.5. Preliminary spectroscopy showed that the cluster in one of the five fields was not sufficiently rich to be interesting, leaving four fields, two from the RCS and two from the SDSS search, whose locations are summarized in Table 1.

2.1. Spectroscopy

2.1.1. Observations

Slit masks for each field were populated with objects from the photometric catalogs, with a slight preference for brighter objects and a strong preference for objects brighter than $r = 22.5$. After the first mask in each field, later masks contained unobserved objects plus a number of already observed objects, most with poor spectra plus some with adequate spectra to use for repeatability tests. Most (39 slit masks) spectroscopy was done with the full 30′ field of the IMACS $f/2$ camera on the Baade Telescope. However, in order to increase the fraction of objects observed in the cluster cores, where slit overlap issues make it particularly difficult to obtain adequate sampling, 3 masks were obtained using the GISMO image slicer (see Dressler et al. 2011) on IMACS, and 16 masks were obtained using the LDSS3 spectrograph on the Clay Telescope, which has an 8.′3 field. Observations were done with a mixture of stare mode and nod-and-shuffle mode. Typical total integration time per mask were in the range of 3–4 hr, divided into individual integrations of 30–45 minutes. All IMACS and LDSS3 spectroscopy, except for the low dispersion prism (LDP) observations discussed below, were made at a dispersion of about 2 Å pixel^{-1}, resulting in a spectral resolution of about 6 Å. Typical image quality during the spectroscopic and imaging observations was 0.″6–0.″8.

The first few slit masks in each field were observed with no band limiting filters, providing spectral coverage between 4300 Å and 9300 Å. Later observations were done with a filter limiting coverage to 4800–7800 Å. The shorter spectra allowed more spectra—about 300—to be packed onto a single mask, but lost coverage of the Hα line at redshifts $z > 0.19$. In order to obtain Hα observations of as many cluster galaxies as possible, one mask per field was devoted to observations of already discovered cluster members through a 1000 Å wide filter centered on Hα at the cluster redshift.

One mask each was obtained in all fields except SDSS1500 with the IMACS LDP. With a mean resolution $\lambda/\Delta\lambda \sim 30$, the LDP spectra cannot be used to measure individual line strengths, but are sufficient to obtain redshifts with a mean accuracy of about 0.01. Because the spectra are very short, of the order of 1000 objects can be observed on one slit mask, to a depth considerably fainter than with grism spectroscopy. More information about the LDP prism can be found in Kelson et al. (2012).

The data sets derived from all of these observations are referred to in the following as the ICBS data sets. For calibration purposes, we also construct a local sample of galaxies with optical spectroscopy, and optical and 24 μm infrared photometry. This sample consists of galaxies with SDSS redshifts between 0.04 and 0.08 located in the three fields of the SWIRE survey (Lonsdale et al. 2003), which are within the SDSS survey area. We take 24 μm flux from the SWIRE observations, and take spectra, redshifts, and optical photometry from the SDSS database.

2.1.2. Spectral Reductions

With the exception of LDP observations, all IMACS and LDSS3 spectra were reduced using the COSMOS data package (Oemler et al. 2011). In general, all observations of an individual mask, whether from one night or from several observing runs were combined into one stack of two-dimensional (flux versus wavelength and slit position) spectral images of individual slits. Using the interactive spectral analysis program VIEWSPECTRA from the COSMOS package, a boxcar one-dimensional extraction of each spectrum was made. Most spectra were extracted over a 1″ length along the slit, but wider extractions were used for particularly diffuse galaxies. LDP spectra were reduced using the methods described in Kelson et al. (2012).

Extracted one-dimensional slit spectra were turned into final calibrated spectra in a three-step process. First, spectra were put onto a relative flux scale by correcting for the instrumental response using observations of spectrophotometric standards. Because the spectral response of IMACS is very stable, a mean spectral sensitivity function for each instrumental setup was derived by combining all standard star spectra taken with this setup. Second, spectra were corrected for atmospheric absorption using the sum of all of the spectra on each slit mask obtained on a given night. Because the galaxies observed on most individual slit masks have a wide range of redshift and spectral type, the spectral features of the individual galaxies are averaged out in this summed spectra, leaving only the spectrum of the atmospheric absorption plus a slowly varying sum of the individual (redshifted) continuum shapes. This spectrum,

after removing the continuum variations, was divided into each galaxy spectrum to remove the atmospheric absorption. Absorption corrections for spectra observed through one of the Hα filters of cluster members could not be performed in this manner, since the wavelength range was too narrow and because all of the objects had similar redshifts. Absorption corrections for these masks were performed using sky absorption spectra obtained from other observations of the same cluster. Third, the spectra are put on an absolute flux scale by scaling their values using the difference between the synthetic r magnitude calculated from each spectrum and the total r magnitude of the galaxy. Assuming that there are no significant color gradients between the roughly $1''$ square area of the galaxy observed with IMACS and the total galaxy, this corrected spectrum represents the total flux of the galaxy. We shall test this assumption later. After calibration, spectra of galaxies obtained from multiple slit masks were combined. We have found that better results were obtained if spectra were combined using a single weight for all data points in spectra from each slit mask, rather than using the pixel-to-pixel statistical weights obtained as part of the reduction process. Relative weights varied by a factor of a few between the best and the worst slit masks. The final quality of the spectra is, of course, quite variable. A small fraction (typically 20%) were too poor to yield a redshift. For the remaining, the median signal-to-noise ratio, per 2 Å pixel, at a rest wavelength of 4500 Å, ranges from 30 at $r = 19.0$ to 7.5 at $r = 22.0$.

Redshifts of galaxies were measured using the cross-correlation method of D. Kelson et al. (2005, private communication). Analysis of repeat observations of galaxies show a typical error $\sigma(z) \sim 2 \times 10^{-4}$. This error is, to first order, independent of spectral type (absorption or emission lines) or galaxy brightness. It is larger than that expected due to the typical wavelength errors determined by measuring atmospheric emission lines $\sigma(z) \sim 6 \times 10^{-5}$, but is comparable to that expected due to slit errors. The location of spectra along the slits show a scatter about the expected position of about 1 pixel, equivalent to astrometric errors in the galaxy catalogs of $0\farcs2$. A scatter of 1 pixel in the centroid of the galaxies in the dispersion direction corresponds to a redshift error $\sigma(z)$ of 3×10^{-4}.

The completeness of the RCS1102 redshift sample, typical of all fields, is presented in Figure 1. The total completeness, shown by the black curve, is the product of two factors: the fraction of objects observed, shown by the red curve, and the rate of success in obtaining redshifts from the spectra, shown by the green curve. Although the success rate declines from almost 100% for the brightest objects to about 75% by $r = 22$, most of the incompleteness is due to object selection, which varies both with magnitude and with position with the field. The decline with magnitude in the fraction of objects observed, from about 70% for bright objects to 55% at $r = 22$, is completely due to the algorithm which selects objects to be included on a slit mask, and which has a mild preference for brighter objects. The spatial variation in completeness is small. Because of the number of masks used in each cluster, and because a concerted effort was made to sample well the cluster core, there is very little under-sampling of objects in groups and the cluster. Typically, what under-sampled regions exist lie near the periphery of the field.

Since it is generally easier to identify redshifts for galaxies with strong emission lines, we have checked for such a bias in our redshift catalog. To minimize evolutionary effects (fainter galaxies tend to be at higher redshift, and SFRs increase with redshift; see Paper III), we examine the fraction of galaxies with EW([O II]) $\geqslant$ 5 Å in the redshift range $0.15 \leqslant z \leqslant 0.35$.

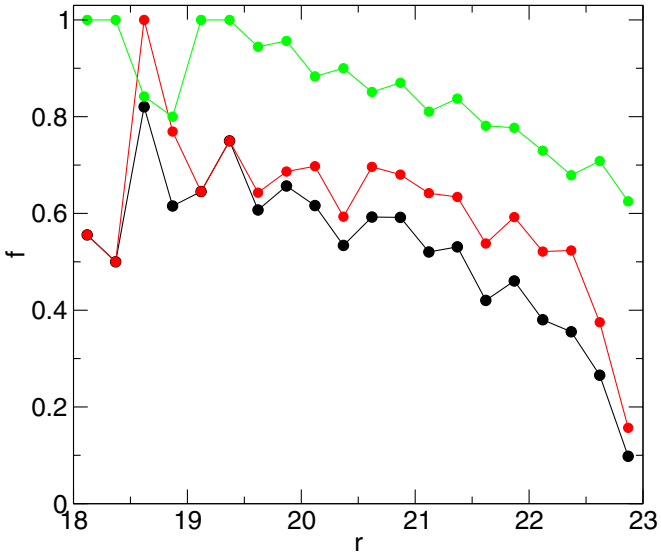

Figure 1. Completeness of the RCS1102 sample. Black line: fraction of catalog with redshifts; red line: fraction of the catalog that was observed; green line: fraction of observed objects that yielded a redshift.

(A color version of this figure is available in the online journal.)

Brighter than $r = 20.5$ absorption spectra increase in frequency, because early-type galaxies dominate the bright end of the luminosity function. However, between $r = 20.5$ and $r = 23.0$, the fraction of emission line galaxies is constant, demonstrating that any spectral type bias is minimal in our sample.

Emission and absorption lines in both the ICBS and SWIRE samples were measured using VIEWSPECTRA. This is a semi-automatic process, in which Gaussian profiles are fit to each line. The wavelength intervals of continuum side bands, and of the line itself, are specified in advance. However, one can interact with the fitting process to correct for less than perfect fits by altering any of the fitting parameters. Output of the fitting includes equivalent widths of emission and absorption lines as well as fluxes of emission lines. Because the spectra have previously been given an absolute calibration, the resulting fluxes represent the total line flux for the entire galaxy.

In fitting Balmer emission lines, an attempt was made to properly set the continuum in the bottom of the stellar absorption line; however, given the typical signal-to-noise ratios of these spectra, there is a limit to how well this can be done. When measuring the Hδ absorption line, no attempt was made to remove contamination from Hδ emission. Because the Hδ line is often of marginal signal-to-noise ratio in these spectra, an improved measure of EW(Hδ) was constructed by combining the Hδ strength with that of the Hϵ line, which lies on top of the Ca H line. Hϵ was determined from the difference between the Ca K line and the Ca H + Hϵ equivalent width. Empirically, it was found that the Hδ equivalent width is related to that of H+Hϵ and K as

$$\begin{aligned} &\mathrm{H-K} < 3\ \text{Å} \quad \mathrm{H}\delta = 1.73 + 0.5(\mathrm{H-K}) + 0.04(\mathrm{H-K})^2 \\ &\mathrm{H-K} \geqslant 3\ \text{Å} \quad \mathrm{H}\delta = 0.77(\mathrm{H-K}) + 1.35, \end{aligned} \tag{1}$$

where H − K is the difference, in Ångstroms, between the equivalent widths of H + Hϵ and K. Our final Hδ values are the average of Hδ and that derived from H and K.

The [O II] line lies in a rather clean spectral region and is easy to measure except for one complication. Some galaxies, even some with very strong [O II], have a very weak stellar continuum at 3727 Å. Slightly incorrect continuum levels in the

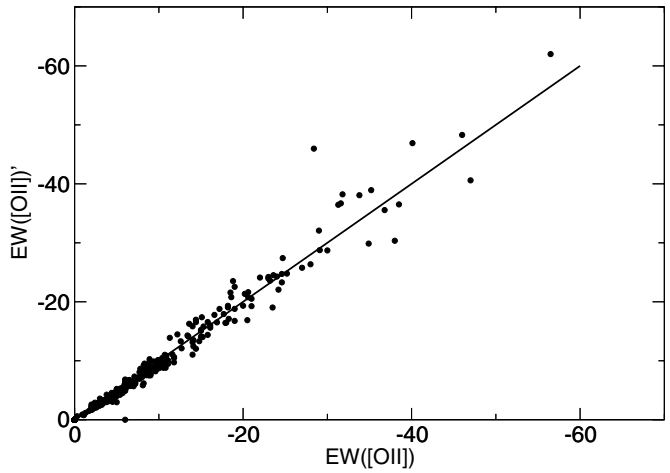

Figure 2. Synthetic EW([O II]), as defined by Equations (2) and (3), vs. directly measured EW([O II]), for objects in the SWIRE sample.

reduced spectra due, for example, to sky subtraction errors, can result in quite large fractional changes in the continuum value, and therefore quite large errors in the equivalent width of [O II]. To avoid this problem, we define a pseudo-continuum at 3700 Å based on an empirical relation between 3700 Å flux and a combination of $M(B)$ magnitude and $B-V$ color, derived from synthetic photometry of the SWIRE sample of SDSS spectra, and from this plus measured [O II] flux, determine EW([O II]). The relation between synthetic and directly measured EW([O II]) is presented, for the SWIRE sample, in Figure 2; a best fit to this relation is:

$$\mathrm{EW([O\,II])} = -1.13 \times 10^{-32} L(\mathrm{O\,II})/10^{-0.4M37}, \qquad (2)$$

where the 3700 Å monochromatic magnitude M_{37} is approximated as

$$M_{37} = M_B + 0.20 + 0.67(B-V-0.09) + 0.0359(B-V-0.09)^2. \qquad (3)$$

Analysis of repeat measurements of individual galaxies show that [O II] and Hβ determinations have typical errors of 0.07 dex, and Hδ determinations have typical errors of 0.13 dex; however, these errors are quite dependent on spectral quality.

The ICBS spectra are typically extracted from an aperture 1″ square, equivalent to a 5.3 kpc square area in a $z = 0.40$ galaxy. This is considerably smaller than the area containing the bulk of stars of the typical luminous galaxy. Since many of the galaxy parameters which we derive depend on an extrapolation from the spectroscopically observed area to the total galaxy, any systematic shift between line strengths in the galactic center to those of the entire galaxy could lead to systematic errors in, for example, SFRs and internal extinction. To test for this, we take two-dimensional spectra from several of the best masks and construct synthetic spectra of an area 3″ in diameter. Figure 3 compares 1″ and 3″ measures of EW([O II]) and EW(Hδ). The synthetic spectra are necessarily quite noisy, resulting in considerable scatter, but it is clear that there in no systematic trend of either with area, indicating that our measured line strengths are reliable indicators of the total galaxy values.

2.2. Photometry

Direct imaging in the griz bands was obtained for the RCS0221 and SDSS0845 fields with the $f/2$ camera of IMACS.

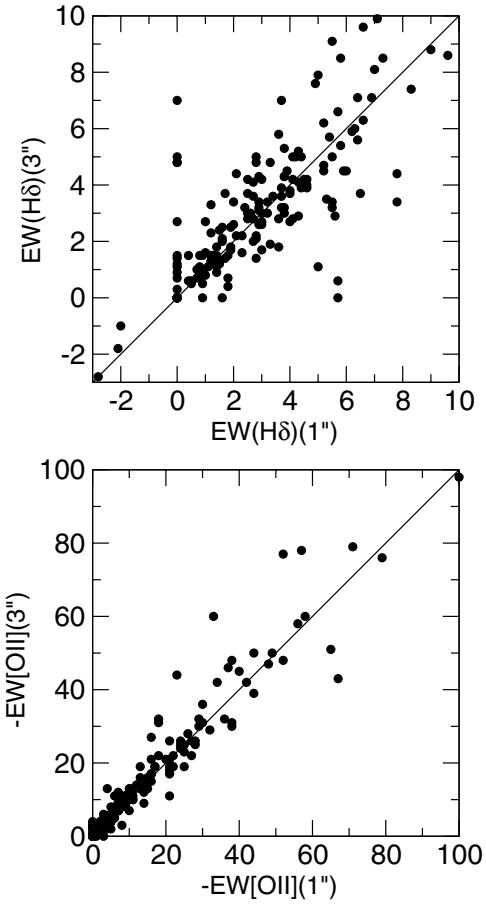

Figure 3. Synthetic 3″ line strengths vs. measured 1″ line strengths, for galaxies in several masks.

Imaging in the *BVRI* bands was obtained for RCS1102 and SDSS1500 using the Wide Field CCD camera on the du Pont Telescope. In addition, very deep *r*-band photometry, complete to $r = 25.0$ was obtained for all fields with IMACS. Photometry of the images was performed using SExtractor (Bertin & Arnouts 1996). Rest frame $B-V$ colors and absolute B magnitudes were derived from the IMACS and du Pont photometry, using *k*-corrections derived from spectral templates constructed from the spectra of SDSS galaxies in the SWIRE sample described above. Typical color errors at (20.0, 22.0) mag are (0.007, 0.04) in $(r-i)$, (0.015, 0.07) in $(i-z)$, (0.05, 0.10) in $(B-V)$, and (0.04, 0.08) in $(V-R)$. For a small number of galaxies with no direct imaging, we have constructed synthetic rest frame colors and absolute magnitudes from the (fluxed) spectra.

The RCS0221 and SDSS0845 fields were mapped by the *Spitzer Space Telescope* (Werner et al. 2004) with the MIPS instrument (Rieke et al. 2004) in the 24 μm band. Data were taken in guest observer program 40387 (PI: Dressler). Including overheads, the observations lasted 11.7 hr per field. For each cluster, the circular 27′ diameter IMACS field of view was tiled with four overlapping MIPS raster-map photometry sequences. This covered the area more efficiently than would scan mapping. For almost all the IMAC field of view, at least two raster-maps overlap, providing $\geqslant$980 s exposure time per pixel for SDSS0845, and $\geqslant$1069 s for RCS0221.

The raw MIPS images were reduced and mosaicked using the MIPS Instrument Team Data Analysis Tool (Gordon et al. 2005). The temporally varying ecliptic foreground was subtracted

separately from each pointing. Photometry at 24 μm was obtained by fitting the point spread function (PSF), using the IRAF implementation of the DAOPHOT task allstar (Stetson 1987). The PSF was created empirically from stars in each cluster, and an aperture correction was applied as in Rigby et al. (2008).

An extremely bright foreground carbon star at α, δ = 08:45:22, +03:27:09 (J2000) contaminates an area $\sim$2.′5 in radius in the cluster SDSS0845. The SDSS0845 catalogs were edited by hand to remove artifacts caused by this star and account for missing survey area obscured by the star. Comparing object counts in our fields with the deep 24 μm counts by Papovich et al. (2004) we determine that our photometry is complete to about 60 μJy, equivalent to a SFR of about 1 $M_\odot$ yr^{-1} at $z \sim 0.4$, with typical errors of about 15 μJy.

3. DATA ANALYSIS

3.1. Determination of Galaxy Properties

3.1.1. Star Formation Rates

The star formation indicators available to us are the optical [O II] λ3727, Hβ, and Hα emission lines, and the 24 μm mid-infrared flux. In principle, the most direct measure of SFRs comes from extinction-corrected hydrogen recombination lines (see, e.g., Kennicutt 1998 for a discussion of the general problem). However, our data is inadequate to determine reliable extinction corrections. Of those methods available to us, many studies have established that using the 24 μm flux is the best choice. A number of empirical calibrations have been made of the correlation of SFR with infrared luminosity. Since most of the mid-IR flux comes from warm dust heated by absorbed UV radiation from H II regions (see, e.g., Wang & Heckman 1996), one would expect the best correlation to be between SFR and the IR bolometric luminosity. However, that is an observationally difficult quantity, and luminosities in either the IRAS 25 μm band or the *Spitzer* 24 μm band are more practical measures. Most studies (e.g., Wu et al. 2005; Calzetti et al. 2005; Alonso-Herrero et al. 2006; Rieke et al. 2009) have looked at correlations between bolometric or 24 μm luminosities and other measures of SFRs. Among the most sophisticated analyses is that of Rieke et al. (2009), who make use of spectral templates to predict 24 μm bolometric corrections, as a function of IR luminosity and as a function of redshift.

However, as Perez-Gonzalez et al. (2006) have pointed out, the true expected correlation should be between IR luminosity and the *absorbed* rather than total UV luminosity, since only the former heats the dust. Put another way, the correlation should be between the SFR and the sum of the IR luminosity and the *escaped* UV luminosity. Perez-Gonzalez et al. (2006), Calzetti et al. (2007), Kennicutt et al. (2009, hereafter K09) and Calzetti et al. (2010) have all provided calibrations of this relation. All have substituted the easily observed escaped Hα flux for the unobserved UV flux in this analysis. This is not strictly correct, because the ratio of absorbed to escaped radiation is much higher in the UV than it is at Hα. K09 argue that this discrepancy is compensated for by other factors. This is not necessarily true, but the K09 formulation, also used by Calzetti et al. (2010), is more convenient than a more strictly correct analysis, and the best test of its usefulness is the tightness of the correlation between predicted and true SFRs.

We shall use the relations between 24 μm and Hα luminosities and SFR given by Equation (17) of Calzetti et al. 2010, but with a slight modification to remove the discontinuities in their formulation at $L(24) = 4 \times 10^{42}$ and $L(24) = 5 \times 10^{43}$. With this modification, and renormalizing to a Salpeter initial mass function (IMF), we have

$$\begin{aligned} &L(24) < 4 \times 10^{42} && \mathrm{SFR} = 8.1 \times 10^{-42}[L(\mathrm{H}\alpha) \\ &&& \quad + 0.020L(24)] \\ &4 \times 10^{42} < L(24) \leqslant 5 \times 10^{43} && \mathrm{SFR} = 8.1 \times 10^{-42}[L(\mathrm{H}\alpha) \\ &&& \quad + 3 \times 10^{-9} L(24)^{1.16}] \\ &L(24) > 5 \times 10^{43} && \mathrm{SFR} = 2.86 \times 10^{-43} L(24). \end{aligned} \quad (4)$$

In this and all following equations for SFRs, luminosities are in units of erg s^{-1}cm^{-2}, SFRs are in units of $M_\odot$ yr^{-1}, and we assume a mass scale based on a Salpeter IMF.

At higher redshift the Hα line is often not observable, and we have no measurements of it for about two-thirds of our galaxy sample; [O II] is the best substitute. Although the relationship between line strength and SFR is more straightforward with the Balmer lines than with [O II], the higher-order Balmer lines are both weaker than [O II] and also increasingly complicated by underlying stellar absorption lines. Using [O II] instead of Hα in the Calzetti et al. (2010) method should be equally good or better, since the extinction at [O II] is closer to that in the UV. Using the data on normal galaxies from Moustakas & Kennicutt (2006), as tabulated in Table 2 of K09 (hereafter called the K09T2 data set), as well as our own data, we obtain consistency between SFR calculated from $L(24)$ and $L([\mathrm{O\,II}])$ with that calculated from $L(24)$ and $L(\mathrm{H}\alpha)$, with the following set of relations:

$$\begin{aligned} &L(24) < 4 \times 10^{42} && \mathrm{SFR} = 8.1 \times 10^{-42}[1.3L(\mathrm{O\,II}) \\ &&& \quad + 0.020L(24)] \\ &4 \times 10^{42} < L(24) \leqslant 5 \times 10^{43} && \mathrm{SFR} = 8.1 \times 10^{-42}[1.6L(\mathrm{O\,II}) \\ &&& \quad + 3 \times 10^{-9} L(24)^{1.16}] \\ &L(24) > 5 \times 10^{43} && \mathrm{SFR} = 2.86 \times 10^{-43} L(24). \end{aligned} \quad (5)$$

The above relations were derived from low-redshift galaxies. For higher redshift objects, observed $L(24)$ will systematically depart from rest frame $L(24)$, so the application of a k-correction is necessary. Unlike the optical case, where one usually has optical colors with which to calculate the continuum slopes needed to obtain the k correction, mid-IR photometry in adjacent bands is not necessarily available. Instead, we use the tabulated k-corrections by Rieke et al. (2009) which have been calculated from models for star-forming galaxies, which predict the continuum shapes and k-corrections as a function of SFR.

If no information on optical emission lines is available we must fall back on an empirical calibration of SFR versus $L(24)$. Figure 4 presents the distribution of the SFR calculated from Equations (4) or (5) versus $L(24)$ for the K09T2, SWIRE, and ICBS data sets. The black line represents Equations (4) and (5) in the case where $L(\mathrm{H}\alpha)$ and $L(\mathrm{O\,II})$ are zero, expected when galactic extinction is so high that all the UV flux is absorbed and reemitted in the IR. As it should, this line follows the lower envelope of the galaxy data. The green line represents the best fit to the data, and is of the form

$$\begin{aligned} &L(24) < 2.5 \times 10^{42} && \log(\mathrm{SFR}) = 0.81[\log(L24) \\ &&& \quad - 42.40] \\ &2.5 \times 10^{42} < L(24) \leqslant 5 \times 10^{43} && \log(\mathrm{SFR}) = 0.86[\log(L24) \\ &&& \quad - 42.40]. \end{aligned} \quad (6)$$

This relation seems to be valid for galaxies at all redshifts and all 24 μm luminosities within our samples.

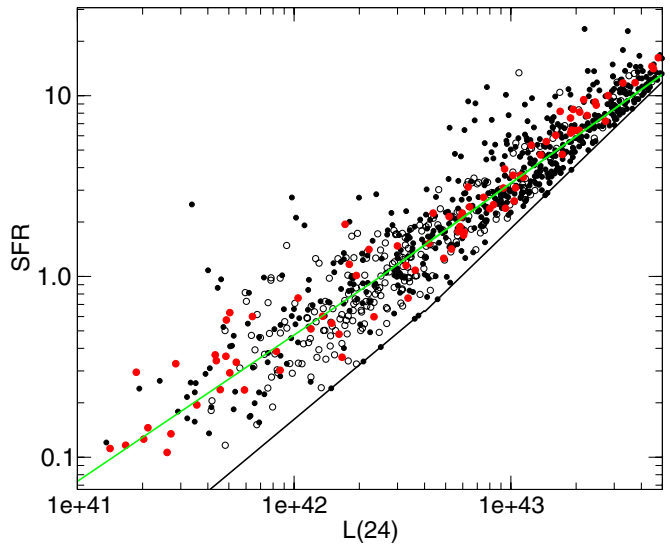

Figure 4. Star formation rate, calculated from Equations (4) and (5) vs. 24 μm luminosity, for galaxies in the K09T2 (red cirlces), SWIRE (open circles) and ICBS (black circles) samples. The green line is a best fit to the data; the black line represents Equations (4) and (5) with no optical emission contribution.

(A color version of this figure is available in the online journal.)

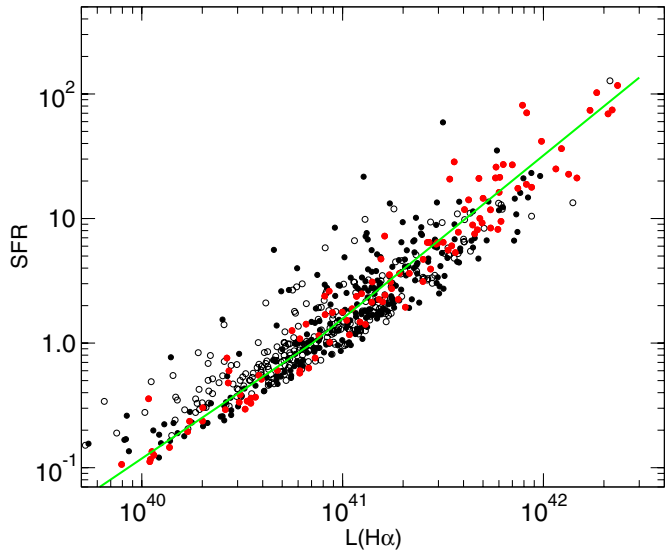

Figure 5. Total star formation rate vs. observed Hα luminosity for galaxies in the K09T2 sample (red points) and in the ICBS (filled points) and SWIRE samples (open circles). The green line is a best fit to the data.

(A color version of this figure is available in the online journal.)

If mid-infrared photometry is not available, the only recourse is optical emission lines. In principle, one should be able to use line ratios to correct these lines for extinction, as has been used to obtain, e.g., $L(\mathrm{H}\alpha)_{\mathrm{tot}}$ for the K09T2 sample. Unfortunately, this requires better data than is usually available for faint galaxies. Experimenting with the ICBS and even the SWIRE data sets demonstrate that using Balmer lines, or Balmer to [O II] ratios to correct the optical line strengths only introduces noise, without improving either random or systematic errors in SFRs. Instead, we will derive empirical relations between observed line luminosities and SFRs.

In Figure 5 we present the relation between SFR and *observed* Hα luminosity, for galaxies, in the K09T2 sample, and in the SWIRE and ICBS samples, where SFRs were calculated

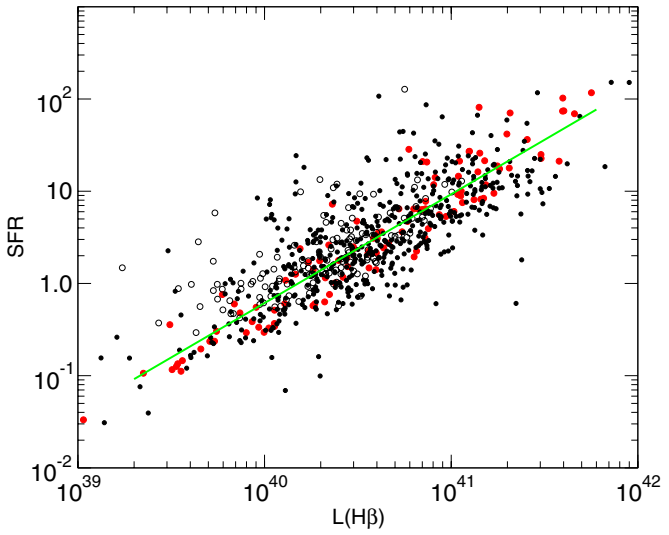

Figure 6. Total star formation rate vs. observed Hβ luminosity for galaxies in the K09T2 sample (red points) and in the ICBS (filled points) and SWIRE samples (open circles). The green line is a best fit to the data.

(A color version of this figure is available in the online journal.)

using Equations (4) and (5). All three data sets show a similar relation between SFR and $L24$; the best solution is shown by the green line. The scatter about the line has a dispersion $\sigma(\log(\mathrm{SSFR})) \sim 0.16$ for the K09T2 sample, and 0.25 for the noisier ICBS data:

$$\begin{aligned} L(\mathrm{H}\alpha) &< 7 \times 10^{40} \quad \log(\mathrm{SFR}) = 1.09(\log(L(\mathrm{H}\alpha)) - 40.85) \\ L(\mathrm{H}\alpha) &\geqslant 7 \times 10^{40} \quad \log(\mathrm{SFR}) = 1.31(\log(L(\mathrm{H}\alpha)) - 40.85). \end{aligned} \tag{7}$$

If Hα is not observable, Hβ is the next best choice. In Figure 6, we present the relation between SFR and observed Hβ luminosity, for the same data sets as presented in Figure 5; the best solution for the ICBS data is

$$\log(\mathrm{SFR}) = 1.18(\log(L(\mathrm{H}\beta)) - 40.18). \tag{8}$$

The scatter in the Hβ determined SFR is larger: $\sigma(\log(\mathrm{SSFR})) \sim 0.25$ for the K09T2 sample, somewhat larger for the ICBS data. Finally, if even Hβ is unobservable, we must fall back on [O II], for which the calibration is presented in Figure 7. The best solution for all the data is

$$\log(\mathrm{SFR}) = 1.10(\log(L(\mathrm{O\,II})) - 40.39). \tag{9}$$

The scatter for [O II] is $\sigma(\log(\mathrm{SSFR})) \sim 0.43$ for all samples.

It must be emphasized that all of these SFR calibrations, and particularly those using only one optical line or IR band, are only claimed to be valid for the SFRs and galaxy types used in the calibration. However, the galaxy sets which we use should fairly sample normal luminous galaxies are redshifts $z \leqslant 1.0$. The similarity in the relations between, for example, the K09T2 and ICBS galaxy samples, which contain galaxies at quite different redshifts, observed in very different manners, gives us some confidence that these calibrations are indeed appropriate for our sample, and for any of the other galaxy samples produced by surveys of the general galaxy population of the universe. They may or may not be equally applicable to unusual objects such as ULIRG's, or to extreme dwarf galaxies, or to objects at very high redshift.

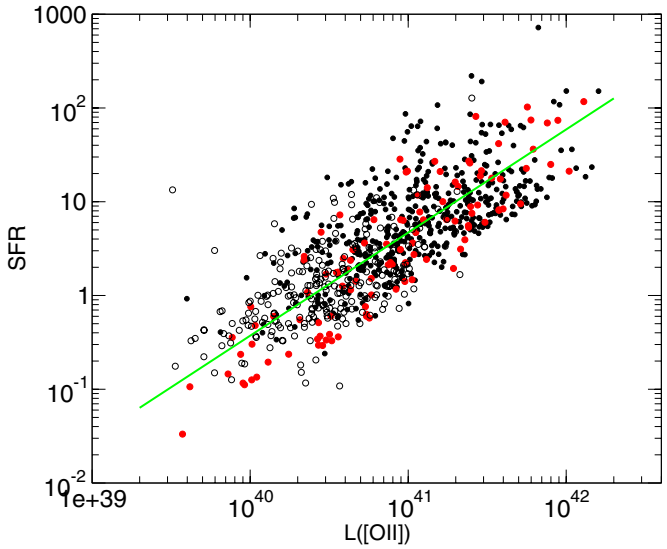

Figure 7. Total star formation rate vs. observed [O II] luminosity for galaxies in the K09T2 sample (red points) and in the ICBS (filled points) and SWIRE samples (open circles). The green line is a best fit to the data.

(A color version of this figure is available in the online journal.)

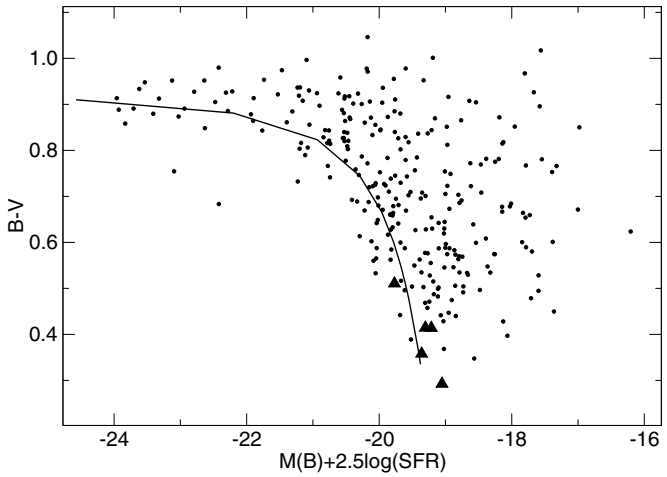

Figure 8. Observed rest frame $B-V$ colors of galaxies in the SWIRE sample vs. the quantity $M(B)$+2.5 log(SFR). Large triangles are objects with $A(V) \leqslant 0.35$. The solid line is the predicted relation for delayed exponential models.

3.1.2. Internal Extinction

For those galaxies with detected 24 μm flux, and detected [O II] or Hα flux, we can calculate $AV_{\rm em}$, the extinction toward the emission line regions, from the ratio the SFR calculated from Equations (4) or (5), and that obtained from the same equations in the limit of $L(24) = 0$, i.e., the case of zero extinction. However, sometimes it will be useful to know the extinction toward the total stellar continuum of a galaxy. (For example, in Section 3.2 we shall use the dereddened galaxy colors as a starburst criterion). We determine this by the method described below, using the SWIRE data set. Figure 8 presents the relation, for objects in this sample, between the observed rest frame $B-V$ colors and the quantity SFRM $\equiv M_B + 2.5\log(\mathrm{SFR})$, i.e., the SFR per unit blue luminosity in magnitude form. Objects with emission line extinctions $AV_{\rm em} \leqslant 0.35$ are shown as large triangles. The solid line is the prediction of a set of galaxy models computed with the Padova evolutionary tracks (Bertelli et al. 1994), adopting a Salpeter IMF with masses in the range

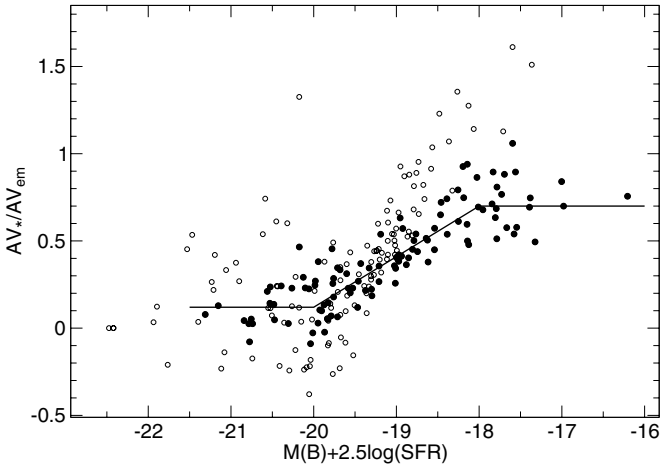

Figure 9. Ratio of AV_* to $AV_{\rm em}$ vs. $M(B)$ + 2.5 log(SFR), for objects in Figure 8. Open circles: all objects; filled circles: objects with $AV_{\rm em} \geqslant 1.0$, which should have more reliable values of $AV_*/AV_{\rm em}$. The solid line is the relation summarized in Equation (11).

0.15–120 $M_\odot$, and with star formation histories following the form introduced by Gavazzi et al. (2002):

$$\mathrm{SFR} \sim \frac{t}{\tau^2} e^{-t^2/2\tau^2}. \quad (10)$$

We shall call these *delayed exponential* models. These models use the observed stellar libraries of Jacoby et al. (1984) in the optical (~3400–7400 Å), and they were extended to the ultraviolet and infrared with the theoretical libraries of R. L. Kurucz (1993, private communication). They include emission lines formed in H II regions, that were calculated using the photoionization code CLOUDY (Ferland 1996). The nebular component was calculated assuming *case B recombination*, electron temperature of 10^4 K and electron density of 10^2 cm^{-3}. The source of ionizing photons was assumed to have a radius of 15 pc and a mass of $10^4\,M_\odot$.

Galaxies with low extinction lie close to the line; all others are redder and fainter (more positive values of SFRM) than the line, as would be expected due to extinction of the stellar continuum. We assume that each galaxy is reddened and dimmed by an amount necessary to move it, along a direction parallel to the reddening vector, from a location along the line to its current position. We call the V band extinction of the galactic stellar population, determined in this way, AV_*, and in Figure 9 present, for the objects in Figure 8, the ratio of $A(V)_{\rm em}$ to AV_*, versus SFRM. This ratio of the extinction toward the stellar population to that toward emission line regions has been extensively studied by Calzetti, who finds an average value of 0.5 (Calzetti 2001). For those galaxies with well determined ratios (i.e., those with significant values of $A(V)$), there is a remarkably tight relation between $AV_*/AV_{\rm em}$ and SFR per *observed* luminosity. Galaxies with weak star formation have low ratios of $AV_*/AV_{\rm em}$, in other words most of the extinction is close to the H II regions, while in galaxies with vigorous star formation the extinction is spread throughout the galaxy.

There is a simple explanation of this. Let us make two (oversimplified) assumptions: (1) all dust is associated with star-forming regions, and (2) the star-forming regions are distributed over the volume of the galaxy in the same way as the stars. Therefore, the average path length for a photon exiting the galaxy will be the same for emission line and continuum photons. Now, if f is the number of star-forming regions along

Table 2
Polynomial Coefficients for M/L_B versus $B-V$

Redshift	a_0	a_1	a_2	a_3	a_4	a_5
0.00–0.25	−4.23	+34.65	−121.05	+220.29	−197.31	+69.03
0.25–0.55	−1.60	+ 6.86	−9.35	+5.22		
0.55–1.00	−1.78	+8.15	−12.41	+7.28		

the line of sight of a photon departing the galaxy, then the number of dust clouds encountered by a photon from an H II region within a star-forming region on the way out of the galaxy is $P_{\rm em} \sim 1 + f$, while the number of dust clouds encountered by photons from a star in the general galaxy population is $P_* \sim f$. Thus, $AV_*/AV_{\rm em} = P_*/P_{\rm em} \sim f/(1+f)$, which goes from 0 for small f to unity for large f. While an undoubted oversimplification, a qualitatively similar trend must exist as long as some fraction of the galactic dust is associated with star-forming regions, which we know is true.

The solid line in Figure 9 is the relation:

$$\begin{array}{ll} \mathrm{SFRM} < -20 & r = 0.12 \\ -20 < \mathrm{SFRM} < -18.1 & r = 0.12 + 0.305(\mathrm{SFRM} + 20) \\ \mathrm{SFRM} > -18.1 & r = 0.70. \end{array} \quad (11)$$

3.1.3. Mass Determination

Bell & de Jong (2001) present simple prescriptions, based on Bruzual & Charlot (2003) population models, for determining the mass-to-light ratios of galaxies from optical broadband colors. As they point out, their prescription for rest frame $B-V$ colors, for galaxies with a Salpeter IMF and solar metallicity: $\log(M/L_B) = -0.51+1.45(B-V)$, has the great virtue that it is almost parallel to the standard reddening vector. Thus, although mass-to-light ratios derived by this method are very sensitive to galactic extinction, *masses* are not since they are the product of two quantities, $L_{\rm gal}$ and $(M/L)_{\rm gal}$ with almost exactly inverse dependence of extinction. If the predictions of such population models are close to correct, our derived masses will be as well. The most important dependence in such models is on the IMF, and we make the same assumption in calculating masses—a Salpeter IMF, as we have made in calibrating SFRs.

We use a variant of the Bell & de Jong approach, but calculate mass-to-light ratios using the delayed exponential models described in the previous section. We calculate the predictions at the epochs observed at redshifts between 0.0 and 1.1; the results are presented, in comparison with the Bell & de Jong prescription, in Figure 10.

Our results are similar to those of Bell & de Jong, but they vary with epoch, and a linear relation is not the best representation. Instead, we use the polynomials of the form $\log(M/L_B) = \sum_0^n a_i(B-V)^i$, with values of a_i presented in Table 2.

These polynomials do not reflect the full upturn seen in the models at the red end. This is deliberate; given errors in the observed colors, a relation as steep as the model curves would produce much too large values of M/L for some galaxies. Since these relations are not exactly parallel to the reddening vector, we correct both M/L and $L_{\rm gal}$ for extinction before calculating masses. If a continuum extinction value is not available for a galaxy, we assume a value $A(V)_* = 0.4$. Because the above relations are close to the reddening line, the effect of incorrect extinction values on the derived masses will be small.

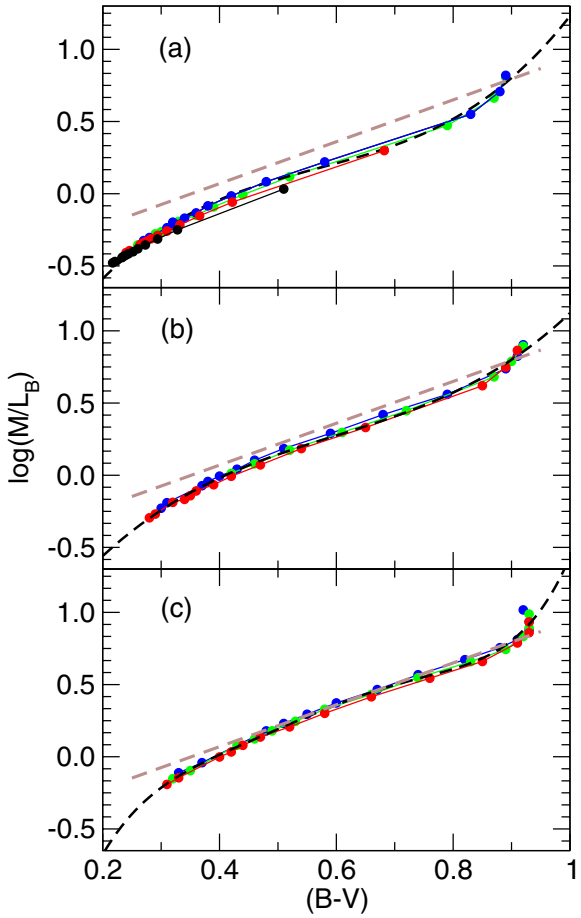

Figure 10. B-band mass-to-light ratios vs. $(B-V)$ color. The brown line represents the Bell & de Jong (2001) solution $\log(M/L_B) = -0.51 + 1.45(B-V)$. The dashed black lines are fits to the delayed exponential model predictions, shown by colored points and lines, in each redshift range. (a) Redshifts of 0.6 (blue), 0.7 (green), 0.9 (red), and 1.1 (black). The fit is to only the 0.6 and 0.7 relations. (b) Redshifts of 0.3 (blue), 0.4 (green), and 0.5 (red). (c) Redshifts of 0.0 (blue), 0.1 (green), and 0.2 (red).

(A color version of this figure is available in the online journal.)

3.2. Starburst Criteria

The role that starbursts might play in the evolution of galaxy populations, both in clusters and the field, has been a subject of considerable attention and controversy, at least since Dressler & Gunn (1983). Papers II and III of this series (Dressler et al. 2013; Oemler et al. 2013) will examine the evidence provided by this survey in some detail. The ICBS data provide multiple means of detecting starbursts. We first reexamine the usual spectroscopic indicators. The equivalent widths of [O II] λ3727 and Hδ have been used for many years as starburst indicators, (e.g., Dressler & Gunn 1983; Couch & Sharples 1987; Dressler et al. 1999); too strong an [O II] line can only be produced in galaxies during a starburst, and too strong a Hδ line is produced either during or after a starburst.

We wish to recalibrate the threshold strengths of both lines which separate normal from bursting star formation, using stellar population models and empirical evidence. The behavior of [O II] is fairly simple to understand. Its equivalent width is the ratio of the emission produced by H II regions to the nearby stellar continuum, to which stars of all ages contribute, but younger, hot stars contribute the most. Dust extinction can only produce one possible effect: selectively diminishing the H II emission line strength relative to that of the more broadly

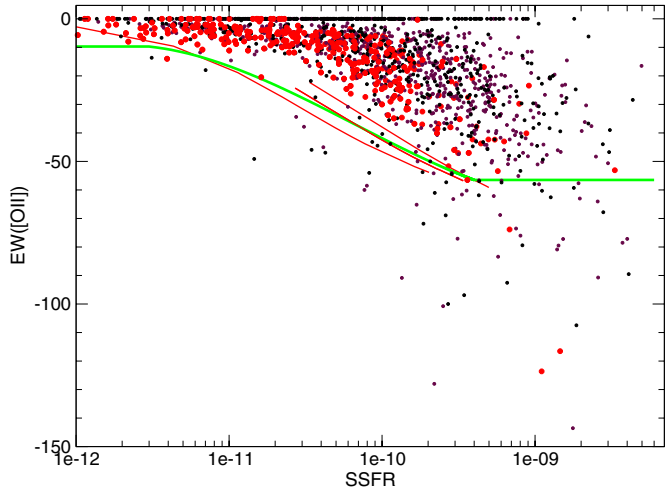

Figure 11. EW([O II]) vs. specific star formation rate. Red points: galaxies from SWIRE and K09T2; black points: ICBS galaxies. Red lines are the relations predicted by our models for redshifts of (top to bottom) 0.0, 0.5, and 1.0. The green line is the adapted threshold for starbursts.

Table 3
Polynomial Coefficients for EW([O II]) versus SSFR

SSFR	a_0	a_1	a_2	a_3
$<3\times10^{-12}$	−10			
3×10^{-12}–4×10^{-10}	3940	1126	123.2	4.033
$\geqslant4\times10^{-10}$	−56			

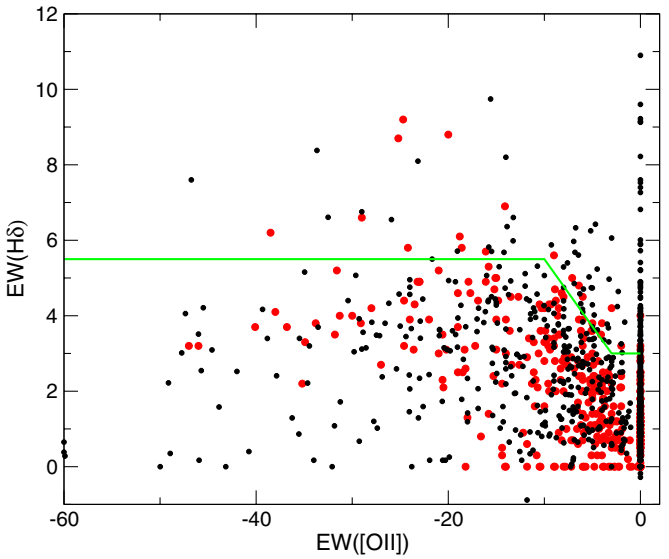

Figure 12. (a) EW(Hδ) vs. EW([O II]) for galaxies in the SWIRE (red points) and ICBS (black points) samples. The green line defines ΔEW(Hδ) = 0.

distributed blue stars. Figure 11 presents the EW([O II]) versus specific star formation rate (SSFR) distribution of galaxies in the SWIRE and K09T2 samples, and of ICBS galaxies. The red lines are the predictions of the extinction-free delayed exponential models for normal galaxies at redshifts (bottom to top) of 0.0, 0.5, and 1.0. These predictions can be taken as maximum allowed values of EW([O II]), since selective extinction of star-forming regions, as described in Section 3.1 will generally reduce the observed value of EW([O II]) below its extinction-free value. We take as the threshold for starbursts the green line, which has the form EW([O II]) $= \sum_0^n a_i(\log(\mathrm{SSFR}))^i$, with values of a_i as presented in Table 3. Necessarily, an O II criterion for starbursts must miss a significant fraction of them, since objects which start off far from the green line may not cross the threshold during even a strong starburst.

The effect of extinction on the Hδ line is more complex and has been studied in some detail by Poggianti et al. (2001). In a dust-free system, Hδ will be strongest in systems dominated by A stars—such as post-starburst galaxies in which the OB stars have died but the A stars have not. In systems dominated by older, cooler stars the line is weaker, in younger, hotter systems the line begins to be filled in by H II region emission. The effect of adding dust will depend on the relative distribution of dust, H II regions, A stars, and cool stars, and may either enhance or diminish the strength of the Hδ line. Some starbursts are known with no visible optical emission lines but strong Hδ (Smail et al. 1999; Dressler et al. 2009), presumably cases where the H II regions are heavily absorbed, but the A star products of the starburst have migrated away from the dustiest regions.

Because of the complexities, a theoretical prediction of Hδ strength is impossible for any but dust-free systems. For galaxies with significant Population I, an empirical determination is necessary. Hδ correlates equally well with [O II] strength and with broadband color; we choose, following previous practice, to use [O II]. In Figure 12 we present the dependence of Hδ on EW([O II]) for galaxies in the SWIRE and ICBS samples. Because there is no reliable theoretical prediction, and because the distribution is broad, we define a measure ΔEW(Hδ), which is the strength of Hδ relative to the line defined in Figure 12, with values, EW([O II]) <= 3.0 Å : EW(Hδ) = 3.0; EW([O II]) > 10 Å : EW(Hδ) = 5.5, and a linear increase between the two.

The quantity ΔEW(Hδ) is a measure of the likelihood that an object is a starburst; within the SWIRE sample about 95% of objects have values of ΔEW(Hδ) less than zero. As with our [O II] measure, the ΔEW(Hδ) criterion will necessarily miss some fraction of starbursts in galaxies whose initial location in the [O II]–Hδ plane is far from the ΔEW(Hδ) = 0 line. However, unlike our O II measure, there will be, at any positive value of ΔEW(Hδ), some chance that the object is *not* a starburst, but merely an outlier in the [O II]–Hδ distribution. For dust-free passive galaxies we can have more confidence; theoretical models (Poggianti et al. 1999) agree with empirical evidence that 3 Å is an upper limit to the Hδ strength of normal galaxies.

Larson & Tinsley (1978) were the first to demonstrate that the color distribution of starburst galaxies is broader than that of normal objects. In Figure 13 we plot the distribution of rest frame $B-V$ colors, corrected for extinction as described in Section 3.1.2 versus SSFR for galaxies in the MK06 and SWIRE samples, and, as a green line, our delayed exponential model predictions for a redshift of 0.0. (At higher redshifts, the predictions for high values of SSFR move parallel to the $z = 0.0$ locus, extending the line to higher SSFR's and bluer colors.) We have determined morphological classifications for as many as possible MK06 galaxies, using images from the NASA Extragalactic Database, and have identified active galactic nuclei (AGNs) using the line strength criteria of Kauffmann et al. (2003). Galaxies which are morphologically and spectroscopically normal are displayed as large black circles; AGNs and morphologically peculiar galaxies are displayed as red circles. SWIRE galaxies, for which no morphology information is available, are shown as small blue circles.

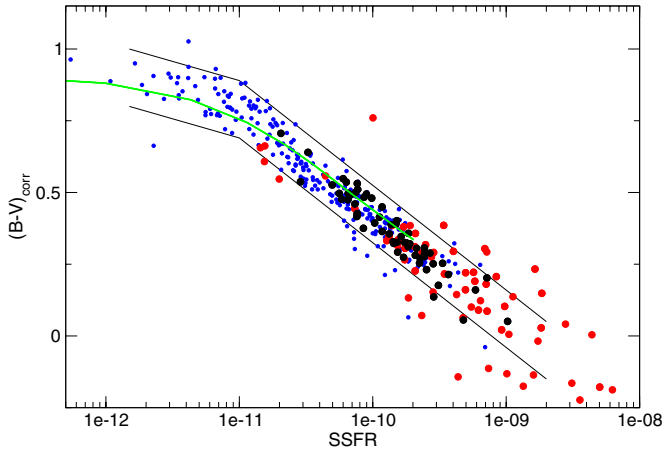

Figure 13. The distribution of reddening-corrected rest frame $B-V$ colors of galaxies in the MK06 and SWIRE samples, vs. specific star formation rate. Green line: predicted relation. Blue points: SWIRE galaxies; black points: normal MK06 galaxies; red points: MK06 galaxies with either morphological peculiarities or spectral indicators of AGN activity. The black lines are our chosen limits for normal galaxies.

Normal galaxies have a very tight distribution about the predicted relation, with $\sigma(B-V)_{\rm corr} = 0.035$. On the other hand, as Larson & Tinsley originally demonstrated, peculiar galaxies—almost all of which have morphological peculiarities suggestive of interactions, and therefore of starbursts, scatter more widely. The two black lines, containing the region of normal galaxies, have the following form, where $S = \log(\mathrm{SSFR}) + 11$:

$$\begin{aligned} S<0: \quad & (B-V)_{\rm min} = 0.69 - 0.13S \quad (B-V)_{\rm max} = 0.89 \\ & \qquad\qquad\qquad\qquad\qquad\quad -0.13S \\ S\geqslant 0: \quad & (B-V)_{\rm min} = 0.69 - 0.315S \, (B-V)_{\rm max} = 0.89 \\ & \qquad\qquad\qquad\qquad\qquad\quad -0.315S. \end{aligned} \tag{12}$$

Objects beyond the region defined by these lines are presumed to be in some phase of a starburst. Objects above the top line, with SFRs too high for their colors, are likely young starbursts. Those below the bottom line, with colors too blue for their SFRs, are probably young post-starbursts. Only about one-third of the morphologically defined starburst candidates lie beyond the normal region. As with the previously defined O II and Hδ starburst indicators, color selection can only discover a fraction of starbursts. Since most of the outliers have very high SSFRs, it will be predominantly the stronger starbursts which are detected by this criterion.

3.3. Cluster Properties

Figure 14 presents redshift–declination pie diagrams for galaxies in the four fields in the redshift interval 0.10–0.80. The RCS0221 and SDSS0845 fields each contain one dominant cluster, at redshifts near where the Red Cluster Sequence cluster detection method predicted one to lie. The situation in the other two fields is more complicated; in both there exist two clusters of comparable richness, and with redshifts similar enough that both probably contributed to the RCS detection signal. Pie diagrams in the redshift region of each of the six major clusters are presented in Figure 15. Filled circles represent objects that we identify as belonging to the clusters. There is, of course, some ambiguity about the correct redshift cut in some of these clusters; we have chosen to err on the side being too inclusive, so as not to miss any potential cluster members in our later analysis, and so as not to contaminate our field sample by cluster members.

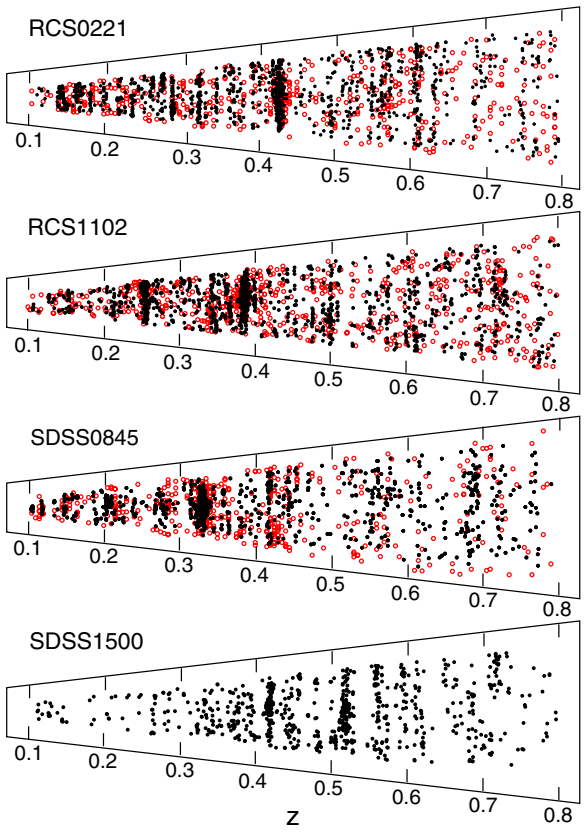

Figure 14. Redshift–declination pie diagrams for each of the four fields. Objects with redshifts determined by grism spectroscopy are shown as black points; objects with only LDP spectroscopy are shown as open red circles.

Table 4
Properties of Clusters

Cluster	$N_{\rm gal}$	z	r_{200} (Mpc)	$L/L*$	σ_{r200}	$\sigma_{\rm tot}$
RCS0221	245 (337)	0.431	1.27	158	941	895
RCS1102A	156	0.255	...	...	...	...
RCS1102B	245	0.386	1.39	224	772	697
SDSS0845	278 (383)	0.330	1.43	202	1087[a]	1031[a]
SDSS1500A	113	0.420	1.17	82	798	639
SDSS1500B	160	0.518	1.23	182	844[b]	904[b]

Notes.
[a] Only includes redshift range 0.317–0.343.
[b] Only includes redshift range 0.507–0.531.

With the cluster membership as defined, Table 4 presents a summary of cluster properties. Numbers in parentheses include LDP spectra. The radius r_{200} is defined in the usual way (Carlberg et al. 1997), σ is the velocity dispersion of all cluster members within a projected radius of r_{200}, $N_{\rm gal}$ is the observed number of members, and $L/L*$ is the total cluster luminosity, in units of $L*$, calculated assuming a Schechter luminosity function with the parameters, $\alpha = -1.05$ and $M_B* = f(z)$ as we determine in Paper III, and correcting for sample incompleteness as a function of magnitude and position. The quantity $L/L*$ should not be over-interpreted: it refers to a volume large compared to either the virial radius or the typical radius to which clusters are normally observed, and therefore

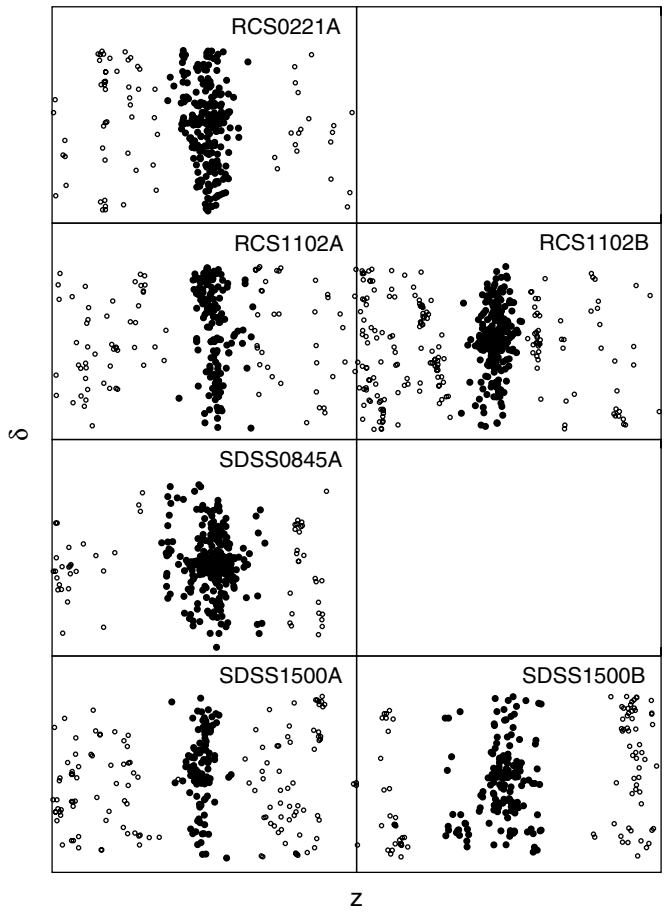

Figure 15. Redshift–declination pie diagrams centered on each of the six massive clusters found in the four fields. Objects with only LDP redshifts are not included. Open circles are field galaxies; filled circles are galaxies assigned to the clusters. The redshift range in each plot is $z_{\rm cluster} \pm 0.07$, the declination range is $0\overset{\circ}{.}7$.

includes much supercluster population. Values are not given for some properties of RCS1102A: the cluster center apparently lies close to the edge of the survey area, and we cannot know what fraction of the total cluster is observed.

4. SUMMARY

We have obtained photometry and usable spectra of 6002 galaxies in four fields of $30'$ diameter, from which were measured absolute magnitudes, rest frame colors, redshifts and absorption and emission line strengths. The 6002 galaxies includes 1394 members of five clusters. Deep 24 μm *Spitzer* photometry was also obtained for two of the four fields. Using new calibrations of SFRs from optical and IR indicators, SFRs, or an upper limit were obtained for 96% of the galaxies in the redshift sample (71% detected SFR, 25% upper limits). From colors, masses were determined for 87% of galaxies with $z \leqslant 0.7$. In addition, at least one measure of the presence or absence of an ongoing or recent starburst was obtained for 69% of the redshift sample.

With these data in hand, we shall examine the evolution of the star formation properties of galaxies in the immediately following papers. Paper II (Dressler et al. 2013) begins the examination of the processes driving the evolution of galaxies infalling into clusters. In Paper III (Oemler et al. 2013) we examine star formation in field galaxies out to $z = 0.6$. Paper IV (Gladders et al. 2013) constructs a more detailed model of field galaxy evolution, using the data discussed in Paper III as well as the observed evolution of the SFR density. In forthcoming papers we will elaborate on this model, as well as examine the effect of mergers and interactions on star formation and evolution, the near infrared properties of our galaxy sample, as well as other aspects of the cluster environment.

Oemler and Dressler acknowledge support of the NSF Grant AST-0407343. This work is based in part on observations made with the *Spitzer Space Telescope*, which is operated by the Jet Propulsion Laboratory, California Institute of Technology under a contract with NASA. Support for this work was provided to A.D., A.O., J.R.R., L.B., and G.R. by NASA through an award issued by JPL/Caltech. Support for this work was provided by NASA to J.R.R. through the *Spitzer Space Telescope* Fellowship Program, through a contract issued by the Jet Propulsion Laboratory, California Institute of Technology under a contract with NASA. B.V. and B.M.P. acknowledge financial support from ASI contract I/016/07/0 and ASI-INAF I/009/10/0. This research has made use of the NASA/IPAC Extragalactic Database (NED) which is operated by the Jet Propulsion Laboratory, California Institute of Technology, under contract with the National Aeronautics and Space Administration. We have made extensive use of Ned Wright's Online Cosmological Calculator (Wright 2006).

REFERENCES

Alonso-Herrero, A., Rieke, G. H., Rieke, M. J., et al. 2006, ApJ, 650, 835
Bell, E. F., & de Jong, R. S. 2001, ApJ, 550, 212
Bertelli, G., Bressan, A., Chiosi, C., Fagotto, F., & Nasi, E. 1994, A&AS, 106, 275
Bertin, E., & Arnouts, S. 1996, A&A, 117, 393
Bruzual, G., & Charlot, S. 2003, MNRAS, 344, 100
Butcher, H. R., & Oemler, A. 1978, ApJ, 2219, 18
Byrd, G., & Valtonen, M. 1990, ApJ, 350, 89
Calzetti, D. 2001, PASP, 113, 1449
Calzetti, D., Kennicutt, R. C., Bianchi, L., et al. 2005, ApJ, 633, 871
Calzetti, D., Kennicutt, R. C., Engelbracht, C., et al. 2007, ApJ, 666, 870
Calzetti, D., Wu, S.-Y., Hong, S., et al. 2010, ApJ, 714, 1256
Carlberg, R., Yee, H., & Ellingson, R. 1997, ApJ, 478, 462
Couch, W. J., & Sharples, R. M. 1987, MNRAS, 229, 423
Dressler, A., Bigelow, B., Hare, T., et al. 2011, PASP, 123, 288
Dressler, A., & Gunn, J. E. 1983, ApJ, 270, 7
Dressler, A., Oemler, A., Gladders, M., et al. 2013, ApJ, 770, 62 (Paper II)
Dressler, A., Rigby, J., Oemler, A., et al. 2009, ApJ, 693, 140
Dressler, A., Smail, I., Poggianti, B. M., et al. 1999, ApJS, 122, 51
Ferland, G. J. 1996, University of Kentucky Internal Report, 565
Gavazzi, G., Bonfanti, C., Sanvito, G., et al. 2002, ApJ, 576, 135
Gladders, M., Oemler, A., Dressler, A., et al. 2013, ApJ, 770, 64 (Paper IV)
Gladders, M. D., & Yee, H. K. C. 2000, AJ, 120, 2148
Gladders, M. D., & Yee, H. K. C. 2005, ApJS, 157, 1
Gneiden, O. Y. 2003, ApJ, 582, 141
Gordon, K. K., Rieke, G. H., George, H., et al. 2005, PASP, 117, 503
Gunn, J. E., & Gott, J. G. 1972, ApJ, 176, 1
Henriksen, M., & Byrd, G. 1996, ApJ, 459, 82
Hubble, E. P. 1936, The Realm of the Nebulae (New Haven, CT: Yale Univ. Press)
Icke, V. 1985, A&A, 144, 115
Jacoby, G. H., Hunter, D. A., & Christian, C. A. 1984, ApJS, 56, 257
Kauffmann, G., Heckman, T. M., Tremonti, C., et al. 2003, MNRAS, 346, 1055
Kelson, D., Williams, R., Dressler, A., et al. 2012, ApJ, submitted (arXiv:1201.0783)
Kennicutt, R. C. 1998, ARA&A, 36, 189
Kennicutt, R. C., Hao, C-N., Calzetti, D., et al. 2009, ApJ, 703, 1672 (K09)
Larson, R. B., & Tinsley, B. M. 1978, ApJ, 219, 46
Larson, R. B., Tinsley, B. M., & Caldwell, N. 1980, ApJ, 237, 692
Lonsdale, C. J., Smith, H. E., Rowan-Robinson, M., et al. 2003, PASP, 115, 897
Moore, B., Katz, N., Lake, G., Dressler, A., & Oemler, A. 1996, Natur, 379, 613

Moustakas, J., & Kennicutt, R. C. 2006, ApJS, 164, 81 (MK06)
Oemler, A., Clardy, K., Kelson, D., Walth, G., & Villanueva, E. 2011, http://code.obs.carnegiescience.edu/cosmos
Oemler, A., Dressler, A., Gladders, M., et al. 2013, ApJ, 770, 63 (Paper III)
Papovich, C., Dole, H., Egami, E., et al. 2004, ApJS, 154, 70
Perez-Gonzalez, P. G., Kennicutt, R. C., Gordon, K. D., et al. 2006, ApJ, 648, 987
Poggianti, B. M., Bressan, A., & Franceschini, A. 2001, ApJ, 550, 195
Poggianti, B. M., Smail, I., Dressler, A., et al. 1999, ApJ, 518, 576
Richstone, D. O., & Malmuth, E. M. 1983, ApJ, 268, 30
Rieke, G. H., Alonso-Herrero, A., Weiner, B. J., et al. 2009, ApJ, 692, 556
Rieke, G. H., Young, E. T., Engelbracht, C. W., et al. 2004, ApJS, 154, 25
Rigby, J. R., Marcillac, D., Egami, E., et al. 2008, ApJ, 675, 262
Smail, I., Morrison, G., Gray, M. E., et al. 1999, ApJ, 525, 609
Spitzer, L., & Baade, W. 1951, ApJ, 113, 413
Stetson, P. B. 1987, PASP, 99, 191
van Dokkum, P. G., Franx, M., Fabricant, D., Illingworth, G. D., & Kelson, D. D. 1999, ApJ, 520, 95
Vulcani, B., Poggianti, B. M., Fasano, G., et al. 2012, MNRAS, 420, 1481
Vulcani, B., Poggianti, B. M., Oemler, A., et al. 2013, A&A, 550, A58
Wang, B., & Heckman, T. M. 1996, ApJ, 457, 645
Werner, M. W., Roellig, T. L., Low, F. J., et al. 2004, ApJS, 154, 1
Wright, N. 2006, PASP, 118, 1711
Wu, H., Cao, C., Hao, C.-N., et al. 2005, ApJL, 632, L79
York, D. G., Adelman, J., Anderson, J. E., et al. 2000, AJ, 120, 1579